# Performance Assessment of a Solar-assisted LiBr–$H_2O$ Absorption Cooling System under Mediterranean climatic conditions

Bilal Abdesselam[1], Mohammed Benramdane[1], Abdennour Aliane[1], Mohammed El Amine Chikh[1]

[1]Applied Energy and Thermal Laboratory (ETAP), Department of Mechanical Engineering, Faculty of Technology, Abou Bekr Belkaid University, B.P 119, Tlemcen 13000, Algeria

**Abstract**_A single-effect LiBr–$H_2O$ absorption cooling system driven by solar thermal energy is dynamically evaluated under typical summer climatic conditions of Tlemcen, Algeria, using combined energy and exergy analyses. The system integrates a solar collector field and thermal storage tank to supply heat to the generator, and two solar technologies, flat-plate collectors (FPC) and evacuated tube collectors (ETC), are investigated and compared on an hourly basis. A dynamic model developed in the Engineering Equation Solver (EES) captures real-time variations in solar irradiation and ambient conditions. Model validation against reference numerical data shows good agreement, with deviations below 1.62% for exergetic efficiency and 1.11% for the coefficient of performance (COP). Results indicate that the ETC configuration significantly enhances thermal delivery, providing 25–50% higher cooling capacity during early morning hours and 35–55% higher output during peak solar periods compared with the FPC. The generator heat input is increased by 27–67% over the day when using ETCs; however, the higher operating temperatures lead to a reduction in exergetic efficiency of approximately 10–25%. Exergy analysis reveals that the solar collector is the dominant source of irreversibility, accounting for nearly 79% of total exergy destruction, followed by the generator (≈12%) and absorber (≈6%). Improvement potential analysis identifies optimization of the solar field as the most effective pathway for performance enhancement. Overall, the ETC-based system offers superior cooling capacity and thermal stability under high solar irradiance, making it a favorable configuration for solar-assisted absorption cooling in hot climates.

*Keywords:* Solar-driven absorption refrigeration; LiBr–$H_2O$ system; thermal storage tank; energy and exergy analysis; solar thermal collector comparison.

## 1. Introduction

North Africa and the Middle East constitute one of the highly climate-vulnerable areas globally [1], exhibiting temperature increases nearly twice the global average [2], with projections suggesting warming rates up to three times higher under high-emission scenarios [3]. In Algeria, maximum temperatures are expected to rise by 5.0–8.0 °C by 2100 under the RCP8.5 pathway, a trend that is anticipated to trigger an exceptional escalation in cooling requirements, projected to increase by approximately 2000% by 2050 relative to 2010 levels [4,5]. This rapid growth in cooling demand is already reflected in national electricity consumption patterns [6], which reached 97.2 TWh in 2023, with 98% of generation supplied by fossil-fuel-based power plants [7,8]. The residential sector accounts

for 38% of total electricity use, and air-conditioning systems contribute up to 89% of demand during summer peak periods [9,10]. These dynamics underscore the urgent need to deploy sustainable, energy-efficient cooling strategies to mitigate both rising electricity loads and associated environmental impacts.

Solar absorption cooling systems (SACSs) represent a promising pathway for sustainable thermal management, as they utilize solar heat as the primary driving force for the absorption refrigeration process [11]. By substituting conventional electricity-intensive vapor-compression units, SACSs significantly reduce dependence on grid electricity and fossil-fuel-based energy sources [12]. Their deployment is particularly advantageous in high-irradiation regions such as Algeria, where substantial solar resources can be leveraged to enhance energy security, lower long-term operational expenditures, and support national and international climate commitments, including those outlined in the Paris Agreement [13,14]. Although SACSs typically exhibit higher capital costs and lower coefficients of performance (COP) compared with conventional vapor-compression technologies [15], they offer durable benefits in regions characterized by elevated electricity tariffs and abundant solar insolation. Furthermore, by relying on solar thermal input to meet cooling demands, these systems can ease peak electricity loads and support substantial reductions in climate-warming emissions [16].

The compatibility of the solar-collection technology with the thermal requirements of the absorption process greatly influences the performance characteristics of SACSs [17]. Non-concentrating solar collectors, especially flat-plate collectors (FPCs) and evacuated tube collectors (ETCs), can efficiently power single-effect absorption chillers operate in the 80–100 °C temperature range [18]. In contrast, double- and triple-effect absorption cycles require significantly higher generator temperatures and thus rely on concentrating solar collectors capable of delivering the necessary high-grade thermal energy [19,20].

Among working fluid pairs, $H_2O$/LiBr remains the most prevalent in air-conditioning applications due to its strong thermodynamic performance in the 5–10 °C evaporating temperature range. However, this pair is susceptible to crystallization at low operating temperatures or high solution concentrations, which poses operational challenges [21–22]. The $NH_3/H_2O$ pair, while better suited for sub-zero cooling due to ammonia's favorable vapor pressure characteristics, is less widely adopted in residential cooling systems [23,24] because of its higher operating pressures and additional safety considerations.

The energetic performance of LiBr–$H_2O$ SACSs has been extensively studied. Saleh & Mosa [23] reported that FPCs perform optimally when supplying generator inlet temperatures between 75 °C and 80 °C. In parallel, Gomri [25] demonstrated that hybrid solar/natural gas configurations in Algeria can supply up to 95% of the generator thermal requirement using solar-based input alone. Migla et al. [26] introduced a single-stage LiBr–$H_2O$ SACS incorporating phase-change storage systems and ETCs; their simulations yielded a COP varying between 0.5 and 0.8, with a peak COP of 0.75 at a generator inlet temperature of approximately 90 °C. Further improvements in operational stability were

documented by Zhu et al. [27], demonstrating that integrating phase-change materials (PCMs) into the system mitigates fluctuations in cooling output under variable solar radiation, resulting in an average COP of 0.679. A study by Bouguetaia et al. [28] investigated a hybrid solar system using an aluminum oxide ($Al_2O_3$) nanofluid and pure water as heat transfer fluids to power a water-lithium bromide single-effect absorption chiller. Their results showed that using the nanofluid improved system performance, achieving a peak thermal efficiency of approximately 54% in winter and 36% in summer. In a techno-economic optimization study for residential applications, Salameh et al. [29] found that ETCs outperform FPCs, enabling the system to achieve a COP of 0.793. This enhancement was largely attributed to optimized collector tilt and thermal storage sizing, which ensured a stable thermal supply to the generator. Overall, previous studies consistently highlight that collector technology, thermal storage capacity, and operating conditions are key determinants of the overall efficiency of LiBr–$H_2O$ thermally driven absorption refrigeration systems [30,31].

While energy analysis provides useful information about system performance, it does not account for thermodynamic inefficiencies or the qualitative aspects of energy conversion. Second-law-based exergy analysis offers a more comprehensive assessment by identifying sources of irreversibility and guiding pathways for system optimization [32]. A novel absorption-compression hybrid refrigeration cycle with rectifier heat-recovery was proposed by Rodríguez-Muñoz et al. [33]. Their thorough exergy evaluation showed significant improvements in both energy and exergy efficiencies compared to conventional configurations. Their results further showed that the integrated design markedly reduced overall thermodynamic irreversibility.

Consistent with these findings, the studies of Hasan et al. [34] and Joybari & Haghighat [35] identified the absorber and generator as the primary sources of exergy losses, whereas Kerme et al. [36] highlighted the solar field as a major origin of irreversibility in solar-assisted systems. Conversely, the exergy analysis conducted by Sahli et al. [37] demonstrated that increasing the pressure ratio adversely affects exergy efficiency, although the system maintains operational flexibility at lower generator temperatures. Similarly, Arora and Kaushik [38] reported that reductions in generator temperature enhance exergetic efficiency, albeit at the expense of cooling capacity.

Despite the extensive body of literature addressing the energy and exergy performance of SACSs, hourly dynamic exergy analyses that explicitly account for realistic fluctuations in solar irradiance remain notably limited, particularly for North African climatic contexts. The majority of existing investigations are conducted under steady-state assumptions or employ time-averaged operating conditions, approaches that inherently obscure the temporal evolution of exergy destruction and irreversibility within individual system components. As a consequence, the influence of short-term solar variability on component-level thermodynamic performance, system-wide irreversibility patterns, and optimization potential has not yet been adequately resolved. In addition, comparative exergy-based evaluations of systems integrating FPCs and ETCs under realistic and transient operating conditions

remain scarce, thereby limiting evidence-based guidance for collector selection and system design in hot, high-irradiance regions such as Algeria.

Accordingly, the present study aims to perform a comprehensive energy and exergy analysis of a solar-assisted, single-effect LiBr–$H_2O$ absorption refrigeration system operating under representative Algerian climatic conditions. The central contribution of this work lies in the application of a time-resolved, hourly exergy analysis framework, enabling the dynamic quantification of exergy destruction and irreversibility within the principal system components throughout the diurnal cycle under realistic variations in solar irradiance and ambient temperature. Furthermore, a comparative thermodynamic assessment of system configurations employing FPCs and ETCs is conducted to identify the dominant sources of exergy destruction and to systematically evaluate the impact of collector technology on overall system performance and solar field sizing requirements. Ultimately, the outcomes of this research are intended to support the development of exergy-informed design and optimization strategies, aimed at enhancing exergetic efficiency and reducing solar field size, thereby contributing to the advancement of sustainable and thermodynamically efficient solar-driven cooling technologies for sun-rich, hot-climate regions.

## 2. Physical Model and Modeling Approach

### *2.1. Configuration of the System and Thermodynamic Processes*

The system under investigation is a solar-driven single-effect thermally driven cooling system that utilizes solar heat input to operate a thermally activated refrigeration cycle [22]. SACSs convert incoming solar radiation to usable heat, which in turn drives the absorption refrigeration process. Owing to their ability to utilize low-grade heat, these systems have been extensively applied in large commercial and institutional buildings for air-conditioning and cooling purposes [23].

The absorption refrigeration cycle shares several thermodynamic principles with the conventional vapor-compression cycle; however, it diverges notably in two fundamental aspects. First, whereas vapor-compression systems rely primarily on electrical energy to power the compressor, the absorption cycle utilizes thermal energy as its main driving force, requiring only minimal mechanical input to operate solution pumps. Second, instead of a single working fluid, absorption systems employ a refrigerant–absorbent pair. The absorbent selectively absorbs refrigerant vapor, enabling pressure elevation through liquid-phase pumping rather than mechanical vapor compression. This substitution yields substantially lower mechanical energy requirements and, consequently, greater potential for renewable-energy-driven operation [24].

A schematic illustration of the SACS functioning as a single-effect cycle with a LiBr–$H_2O$ working pair is shown in Figure 1. Auxiliary devices like a cooling tower, a thermal storage tank, solution heat exchangers, circulation pumps, and expansion valves complement the configuration's four main parts, which are the generator, condenser, evaporator, and absorber. A thermal storage tank, which acts as an intermediary buffer and supplies the necessary heat input to the generator, receives the solar

thermal energy that the solar field has collected. In order to maintain thermodynamic stability and guarantee continuous and effective system operation, heat rejection from the absorber and condenser is achieved by a cooling tower with a specialized cooling-water circuit.

The operation begins at the solar collector field, where solar radiation is captured and conveyed to a circulating working fluid (20). This heated fluid flows into a thermal storage reservoir (19), where the accumulated energy is maintained at elevated temperatures. When sufficient thermal energy is available, it is supplied to the generator (11). In order to guarantee continuous operation during times of low solar irradiation, like early morning hours, an auxiliary heater is incorporated into the system. This heater provides the extra thermal input needed to maintain the generator's operating temperature.

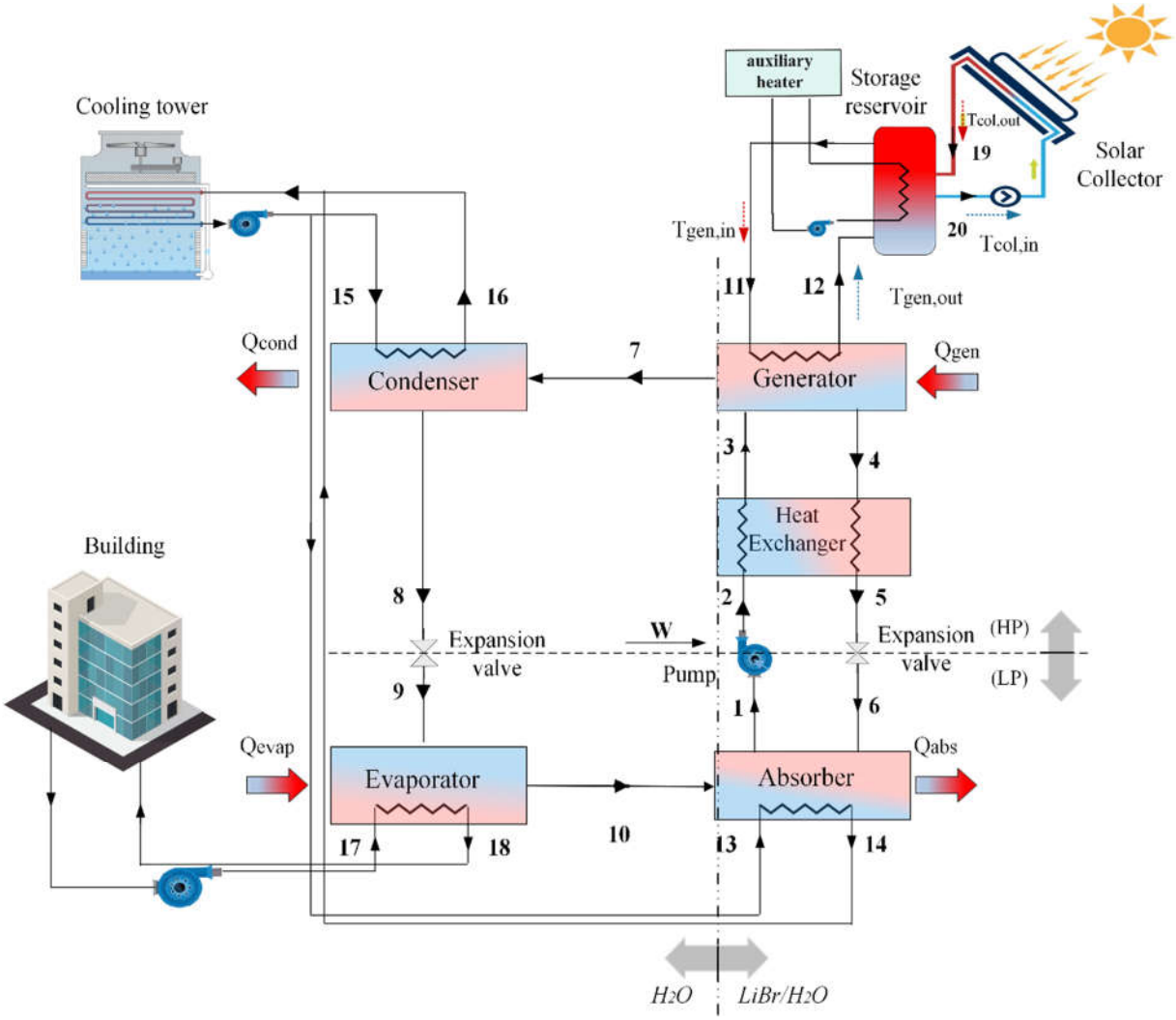


**Figure 1.** Configuration and operating principle of the single-effect SACS.

Heating the LiBr–$H_2O$ solution inside the generator starts the desorption process, which separates the absorbent from the water refrigerant vapor. Refrigerant vapor leaves the generator (7) as the solution temperature rises, leaving behind a high-concentration (strong) LiBr solution (4). Before entering the absorber, this strong solution is pre-cooled in a solution heat exchanger (5) and then cooled by an expansion valve (6).

Concurrently, the generator's high-pressure refrigerant vapor enters the condenser (7), rejecting heat to cooling water provided by the cooling tower. This heat removal causes the vapor to condense into liquid refrigerant (8). The condensed refrigerant then passes through an expansion valve, undergoing a pressure drop before entering the evaporator (9) as a low-pressure mixture. In the evaporator, the refrigerant absorbs heat from the conditioned environment, leading to its evaporation and the production of low-pressure saturated vapor (10).

After entering the absorber (10), the strong LiBr solution absorbs the refrigerant vapor. A weak (diluted) LiBr–H2O solution (1) is formed as a result of the absorption process, which produces heat that is eliminated by the cooling tower water. The thermally powered absorption refrigeration cycle is completed by pumping this weak solution to a higher pressure (2), preheating it in the solution heat exchanger (2–3), and then returning it to the generator.

This integrated configuration enables efficient utilization of solar thermal energy for cooling applications, reducing reliance on conventional electricity-powered systems and offering a sustainable alternative for building climate control.

*2.2. Energy-Based Modeling*

2.2.1. Solar Collector Thermal Performance

In the absorption cooling system, the solar collector is in charge of collecting solar radiation and transferring it to the working fluid as thermal energy. Its performance can be described through the following key aspects:

a- Available Solar Energy

The amount ($\boldsymbol{Q_s}$) of solar radiation ($\boldsymbol{I_T}$) received by the inclined collector surface with an effective area $\boldsymbol{A}_{\text{col}}$ is expressed by the following relation [18]:

$$\boldsymbol{Q_s = A_{col}\, I_T} \tag{1}$$

b- Useful Thermal Energy Gain

The usable heat ($\boldsymbol{Q_u}$), or the amount of solar energy absorbed and transmitted to the working fluid, is expressed as follows [36]:

$$\boldsymbol{Q_u = A_{col} I_T \eta_c} \tag{2}$$

where $\boldsymbol{\eta_c}$ is the collector's thermal efficiency.

c- Total Solar Radiation on a Tilted Collector Surface

The following formula yields the total hourly solar radiation impinge on the collector surface [36]:

$$\boldsymbol{I_T = I_b R_b + I_d R_d + (I_b + I_d) R_r} \tag{3}$$

where:

$\boldsymbol{I_b}$ = beam radiation (W/m²)

$\boldsymbol{I_d}$ = diffuse radiation (W/m²)

For beam, diffuse, and reflected radiation, the corresponding tilt factors are $R_b$, $R_d$ and $R_r$.

d- The Collector's Thermal Efficiency

The quantity of received solar energy ($Q_s$) that the collector converts to useable heat ($Q_u$) is measured by the thermal efficiency [39]:

$$\eta_{col} = \frac{Q_u}{Q_s} = \frac{m_{col}\left(T_{col,out} - T_{col,in}\right)}{A_{col}\, I_T} \tag{4}$$

where $T_{col,in}$ and $T_{col,out}$ are the fluid's inlet and outlet temperatures, and $m_{col}$ is the operational fluid mass flow rate.

e- Collector Type Efficiencies

- FPC:

For the FPC, the standard Greek-type configuration is selected [39]:

$$\eta_{FPC} = 0.75 - 5.0 \cdot \left(\frac{T_{col,in} - T_{am}}{I_T}\right) \tag{5}$$

- ETC:

ETCs outperform FPCs due to vacuum insulation, which minimizes heat losses to the environment [24]. The efficiency of an ETC is given by [40]:

$$\eta_{ETC} = 0.82 - 2.19 \cdot \left(\frac{T_{col,in} - T_{am}}{I_T}\right) \tag{6}$$

Here, $T_{am}$ is the ambient temperature. The choice of collector depends on system requirements, with ETCs preferred for higher efficiency and elevated operating temperatures.

2.2.2. Heat Storage Unit Description

In this work, thermal energy is stored for high-temperature applications using a sensible heat storage device. The system works by heating a liquid that retains energy without undergoing a phase change. Pressurized water is chosen as the working fluid due to its excellent thermophysical properties and its adaptability for elevated temperature operations, ensuring reliable energy storage and delivery.

The core of the system is an insulated storage tank, which receives energy from an array of solar collectors and supplies it to a load as required (see Figure 1). In order to make the analysis simpler, it is assumed that the water in the tank is constantly well-mixed, leading to a consistent temperature $T_s$ that only changes over time. This idealization allows for a straightforward application of energy balance principles.

The rate at which the tank's temperature changes can be represented as follows from an energy perspective [36]:

$$\left[\left(mC_p\right)_s\right]\frac{dT_s}{dt} = Q_u - Q_{load} - (UA)_s(T_s - T_a) \tag{7}$$

where $Q_u$ denotes the useful thermal energy delivered from the solar collectors to the storage tank during a given time step, while $Q_{\text{load}}$ represents the rate of energy extracted to meet the system demand.

Heat losses to the surrounding environment are described by the term $(\boldsymbol{UA})_{\boldsymbol{s}}(\boldsymbol{T_s - T_a})$, where $(\boldsymbol{UA})_{\boldsymbol{s}}$ represents the overall thermal loss parameter of the storage tank, determined from its thermal characteristics. In addition, $\boldsymbol{m}$ represents the mass of water contained in the tank, $\boldsymbol{C_p}$ is the specific thermal capacity of water, and $\boldsymbol{T_a}$ denotes the surrounding environmental temperature around the storage tank.

The Euler integration method can be used to discretize the energy balance equation under the assumption that the energy losses, the useful input $\boldsymbol{Q_u}$, and the load demand $\boldsymbol{Q_{load}}$ stay constant over a time interval $\boldsymbol{\Delta t}$. By discretizing the temperature time derivative as $(\boldsymbol{T_{s,new} - T_s})/\boldsymbol{\Delta t}$, the storage tank temperature at the end of the considered time step is obtained as follows [36]:

$$\boldsymbol{T_{s,new} = T_s + \frac{\Delta t}{mC_p}[Q_u - Q_{load} - (UA)_s(T_s - T_a)} \tag{8}$$

2.2.3. Detailed Absorption Chiller Analysis and Modeling

The thermodynamic assessment of the LiBr–$H_2O$ SACS is performed by applying the mass conservation principle and the 1st law of thermodynamics to each component independently. All system components are represented as control volumes with well-defined inlet and outlet streams, which allows the systematic development of mass and energy balance relationships.

The generator constitutes the reference component for the mass balance analysis. Under steady operating conditions, the mass flow rate entering the generator ($\dot{m}_3$) must equal the sum of the mass flow rates leaving the generator in the form of the weak solution ($\dot{m}_4$) and the refrigerant vapor stream ($\dot{m}_7$):

$$\boldsymbol{\dot{m}_3 = \dot{m}_4 + \dot{m}_7} \tag{9}$$

For LiBr, the mass balance accounts only for the solute portion:

$$\boldsymbol{\dot{m}_3 x_3 = \dot{m}_4 x_4} \tag{10}$$

Subtracting the LiBr mass balance from the total mass balance yields the water mass balance:

$$\boldsymbol{\dot{m}_3(1 - x_3) = \dot{m}_4(1 - x_4) + \dot{m}_7} \tag{11}$$

The energy balance for the condenser establishes a relationship between the heat rejected during vapor condensation and the associated change in enthalpy of the working fluid across the component:

$$\boldsymbol{\dot{Q}_{cond} = \dot{m}_7 h_7 - \dot{m}_8 h_8} \tag{12}$$

Similarly, the generator and evaporator energy balances are expressed as:

$$\boldsymbol{\dot{Q}_{gen} = \dot{m}_7 h_7 + \dot{m}_4 h_4 - \dot{m}_3 h_3} \tag{13}$$

$$\boldsymbol{\dot{Q}_{evap} = \dot{m}_{10} h_{10} - \dot{m}_9 h_9} \tag{14}$$

The absorber energy balance accounts for the heat removed while condensing the refrigerant vapor and mixing with the weak solution:

$$\boldsymbol{\dot{Q}_{abs} = \dot{m}_{10} h_{10} + \dot{m}_6 h_6 - \dot{m}_1 h_1} \tag{15}$$

Within the solution heat exchanger, the energy interaction between the concentrated (strong) and dilute (weak) solution streams is expressed as:

$$\dot{m}_4 h_4 - \dot{m}_5 h_5 = \dot{m}_3 h_3 - \dot{m}_2 h_2 \quad (16)$$

The pump energy balance considers the enthalpy rise due to pressure increase:

$$h_2 = h_1 + (P_2 - P_1)v_2 \quad (17)$$

$$\dot{W}_{pump} = (P_2 - P_1)v_2 \quad (18)$$

The heat exchanger effectiveness ($\varepsilon_{hx}$) is quantified as the ratio between the actual heat exchanged and the maximum achievable heat transfer for the specified inlet conditions:

$$\varepsilon_{hx} = \frac{\dot{Q}_{act}}{\dot{Q}_{max}} = \frac{\dot{m}_4 c_p (T_4 - T_5)}{(\dot{m}c_p)_{min}(T_4 - T_2)} \quad (19)$$

Owing to evaporation within the generator, the heat capacity rate associated with the dilute solution $(\dot{m}_4 c_p)$ is consistently lower than that of the concentrated solution $(\dot{m}_3 c_p)$; consequently, the effectiveness of the solution heat exchanger may alternatively be written as:

$$\varepsilon_{shx} = \frac{(T_4 - T_5)}{(T_4 - T_2)} \quad (20)$$

Energy losses in throttling valves are considered negligible, implying enthalpy conservation across the valve:

$$h_4 = h_5 \quad (21)$$

$$h_7 = h_6 \quad (22)$$

Similarly, enthalpy changes due to pumping of the weak solution are neglected:

$$h_2 = h_1 \quad (23)$$

Neglecting the contribution of pump work, the COP is expressed as the ratio of the cooling effect produced in the evaporator to the thermal energy input supplied to the generator.

$$COP = \frac{Q_{evap}}{Q_{gen}} \quad (24)$$

To assess the SACSs' overall thermodynamic performance, the energy rates of the system components are integrated over the operating period, yielding the daily energy input as follows:

The collector's daily usable energy:

$$Q_{u,day} = \int_{day} Q_u(t).dt \quad (25)$$

The related formulas found in Eqs. (26)–(30), respectively, are used to calculate the daily energy extracted by the condenser, absorber, generator, and evaporator [40]:

$$Q_{cond,day} = \int_{day} Q_{cond}(t).dt \quad (26)$$

$$Q_{abs,day} = \int_{day} Q_{abs}(t).dt \quad (27)$$

$$Q_{gen,day} = \int_{day} Q_{Gen}(t).dt \quad (28)$$

$$Q_{evap,day} = \int_{day} Q_{evap}(t).dt \tag{29}$$

The system's daily thermal efficiency is determined by:

$$\boldsymbol{COP_{day}} = \frac{\boldsymbol{Q_{evap,day}}}{\boldsymbol{Q_{gen,day}}} \tag{30}$$

*2.3. Exergy-Based Modeling*

Exergy analysis provides a powerful tool for optimizing energy utilization by identifying where losses occur, the nature of system inefficiencies, and the magnitude of these losses as the system moves toward equilibrium with its surroundings [41]. In the present analysis, the contributions of kinetic and potential exergy are neglected, and chemical exergy is also assumed negligible due to the absence of any chemical substance exchange between the cycle and the environment. Under these assumptions, the specific exergy of a fluid stream per unit mass can be expressed as [36]:

$$\boldsymbol{\psi = (h - h_0) - T_0(s - s_0)} \tag{31}$$

where ψ denotes the specific exergy, $h$ and $s$ represent the enthalpy and entropy at the considered state, and $h_0$ and $s_0$ correspond to the enthalpy and entropy of the reference environmental state at temperature $T_0$. For this study, the ambient temperature is taken as $T_0 = 298.15$ K. The following relations can be used to determine the total exergy loss for the system as well as the destruction of exergy in each component. The destruction in a single component is given by:

$$\boldsymbol{\dot{E}_{d,ex} = \sum m_{in}\psi_{in} - \sum m_{out}\psi_{out} - Q\left(1 - \frac{T_o}{T_i}\right) - W} \tag{32}$$

where the subscript 'o' denotes ambient conditions, and the subscript 'I' denotes the specific system state of interest. The sum of the destruction of exergy in each of the system's constituent components may then be used to indicate the system's overall exergy destruction:

$$\boldsymbol{\dot{E}_{d,total} = \dot{E}_{d,col} + \dot{E}_{d,st} + \dot{E}_{d,evap} + \dot{E}_{d,shx} + \dot{E}_{d,exp} + \dot{E}_{d,gen} + \dot{E}_{d,abs} + \dot{E}_{d,exp} + \dot{E}_{d,cond} + \dot{E}_{d,pump}} \tag{33}$$

The solar collector's usable energy gain can be calculated as follows [18]:

$$\boldsymbol{\dot{E}_{us} = \dot{m}_{col}c_p\left[(T_{col,out} - T_{col,in}) - T_{amb}ln\left(\frac{T_{col,out}}{T_{col,in}}\right)\right]} \tag{34}$$

According to Petela's theorem, the exergy associated with radiation is expressed as:

$$\boldsymbol{\dot{E}_{ex,in} = A_{col} \times I_t\left[1 + \frac{1}{3}\left(\frac{T_0}{T_s}\right)^4 - \frac{4}{3}\left(\frac{T_0}{T_s}\right)\right]} \tag{35}$$

Where $T_S$ (of 6000 K) represents the sun's temperature. However, this equation can violate the 2nd law of thermodynamics for practical systems. To address this, a corrected form assumes the sun as an infinite thermal reservoir. The exergetic efficiency of the chiller, which quantifies how effectively the system converts input exergy into useful output, is defined as:

$$\eta_{ex,ch} = \frac{\dot{E}_{evap}}{\dot{E}_{gen}} = \frac{\dot{m}_{17}(\psi_{17} - \psi_{18})}{\dot{m}_{11}(\psi_{11} - \psi_{12})} \quad (36)$$

The daily exergetic of the essential system components is evaluated by integrating the exergy rates over the daily operating period, as defined by the following equations [40]:

$$\dot{E}_{evap,day} = \int_{day} \dot{E}_{evap}(t).dt \quad (40)$$

$$\dot{E}_{gen,day} = \int_{day} \dot{E}_{gen}(t).dt \quad (41)$$

$$\dot{E}_{cond,day} = \int_{day} \dot{E}_{cond}(t).dt \quad (42)$$

$$\dot{E}_{abs,day} = \int_{day} \dot{E}_{abs}(t).dt \quad (43)$$

The daily exergitic efficiency can be calculated by dividing Eq. (40) by Eq. (41) and can be expressed as follows:

$$\eta_{ex,day} = \frac{\dot{E}_{evap,day}}{\dot{E}_{gen,day}} \quad (44)$$

*2.4. Modeling Methodology*

A thorough energy and exergy evaluation of a single-effect SACS with two solar collector configurations, FPC and ETC, is presented in this study. The Algerian Meteorological Office's meteorological data for the northern Algerian city of Tlemcen on July 18, 2024, provided representative summer climate conditions, particularly hourly solar irradiance and ambient air temperature. These data were used as inputs to ensure that the simulations accurately reflect typical operating conditions during the cooling season.

The ability of FPC and ETC collectors to supply the necessary thermal energy to the generator of a single-impact absorption chiller, which normally uses a medium-temperature heat source in the range of 80–100 °C [15], was the driving force behind their selection. The collector tilt angle was determined based on the local solar geometry for Tlemcen (latitude 34.9° N) to maximize incident solar radiation and enhance thermal performance.

A vertically oriented cylindrical steel tank serves as the system's thermal storage. The tank is insulated with glass wool, which has a thermal conductivity of 0.04 W/m.K., to minimize heat losses. A dynamic energy balance model was used to calculate the hourly evolution of the storage tank temperature, $T_{s,\text{new}}$. Three main contributions are taken into account by this model: (i) the useful heat obtained from the solar collectors, $Q_u$; (ii) thermal losses to the environment, expressed as $(UA)_s(T_s - T_a)$; and (iii) the heat extracted hourly to supply the absorption chiller generator, $Q_{h,\text{load}}$. The generator's thermal demand profile was used to determine the value of $Q_{h,\text{load}}$ for every hour [42].

The main input parameters used in the simulations, such as the technical details of the solar collectors, absorption chiller, and thermal storage tank, are compiled in Table 1.

**Table 1.** Input parameters and technical specifications used in the simulation.

| Category | Parameter | Symbol | Value |
|---|---|---|---|
| Solar collectors | Slope | - | 23° [1] |
| | Area | $A_c$ | 33.45 m$^2$ [36] |
| | Flow rate of mass | $\dot{m}_{19}$ | 0.05 kg/s |
| | Temperature at the generator's inlet | $T_{11}$ | 95 °C [24,25] |
| Geographical data | Latitude (Tlemcen) | - | 34.88° |
| Thermal storage tank | Volume | - | 2.1 m$^3$ |
| | Coefficient of loss | $(UA)_s$ | 11.1 W/K [36] |
| Hydraulic circuit mass flows | Mass flow rate of the pump | $\dot{m}_1$ | 0.057 kg/s [36] |
| | Flow rate of the generator solution | $\dot{m}_{11}$ | 0.5 kg/s |
| | Water flow rate of the absorber cooling | $\dot{m}_{13}$ | 0.25 kg/s |
| | Flow rate of condenser cooling water | $\dot{m}_{15}$ | 0.28 kg/s |
| | Flow rate of chilled water at the intake | $\dot{m}_{17}$ | 0.3 kg/s |
| Thermal conditions | Absorber cooling water temperature | $T_{13}$ | 27 °C |
| | Condenser cooling water temperature | $T_{15}$ | 27 °C |
| | Temperature of the chilled water inflow | $T_{17}$ | 18 °C |
| Heat exchangers | Solution heat exchanger effectiveness | $\eta_{ex,ch}$ | 0.64 |
| | Condenser UA-value | $UA_{cond}$ | 1.2 kW/K |
| | Evaporator UA-value | $UA_{evap}$ | 2.25 kW/K |
| | Absorber UA-value | $UA_{abs}$ | 1.6 kW/K |
| | Generator UA-value | $UA_{gen}$ | 1 kW/K |

This work offers a thorough analysis of the effects of collector type, ambient temperature fluctuations, and thermal storage properties on the system's energy and exergy performance. This enables the identification of the most suitable solar collector technology and the assessment of the effectiveness of the storage subsystem. Unlike many previous studies, which often neglect the influence of hourly meteorological fluctuations, the variable efficiency of solar collectors, and the performance dynamics of thermal storage under fluctuating loads, this study emphasizes the necessity of evaluating system behavior over an entire diurnal cycle. Such an approach is especially important in regions like North Africa, where high solar irradiance coincides with peak cooling demand, offering favorable conditions for solar-assisted air conditioning.

A rigorous analysis of these hourly variations is essential for accurately characterizing the real operational behavior and reliability of solar-driven absorption systems. This dynamic methodology yields a more realistic appraisal of system efficiency and sustainability under actual working conditions.

*2.5. Code Verification*

The accuracy of the numerical model proposed in this work were validated through a direct comparison of its predictions with the reference results presented by Kerme et al. [36]. The comparison, presented in Figure 2, examines three major performance indicators of the absorption cooling cycle, namely the COP, the $\eta_{ex,ch}$, and the $Q_E$, as functions of the $T_{gen}$. As demonstrated, the current model accurately replicates the trends found by Kerme et al. [36].

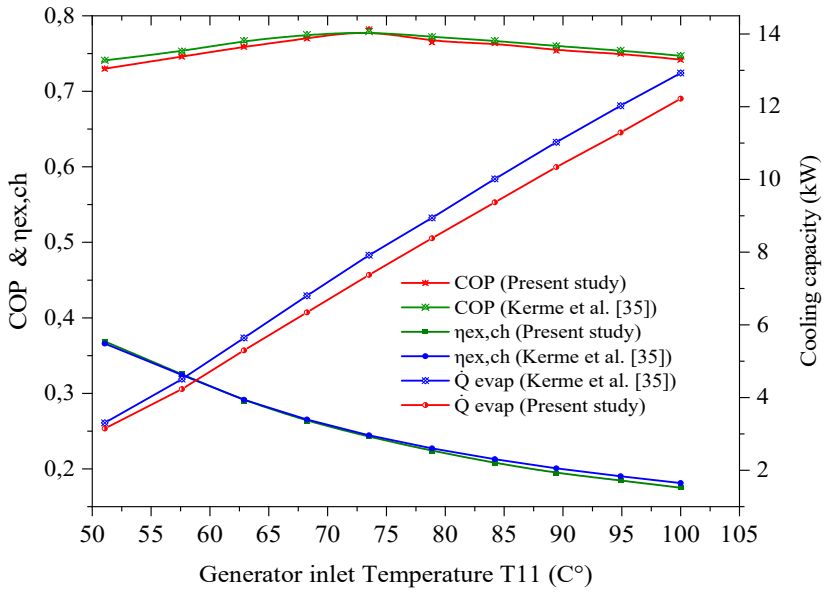


**Figure 2.** Verification of thermodynamic performance parameters against Kerme et al. [36].

## 3. Findings and Discussion

*3.1. Daily Performance of the SACS*

This part uses hourly climatic data to assess the system's daily thermodynamic performance. With preheated storage starting at 07:00, the system, which consists of solar collectors, a thermal storage tank, and a single-effect chiller, is simulated for an entire day. With an emphasis on contrasting FPC and ETC in satisfying the generator's thermal demand under dynamic settings, key parameters are tracked to evaluate energetic and exergetic behavior.

The plots in Figure 3 show a distinct daily pattern in useful heat gain that closely follows the rise and fall of solar irradiance and ambient temperature ($T_{amb}$) in Tlemcen on July 18, 2024. No useful heat is produced before 07:00. Once solar input becomes sufficient, the ETC immediately outperforms the FPC. At 07:00, the ETC provides 621 W compared to 110 W from the FPC, representing an increase of about 464%. This performance gap remains substantial throughout the morning; for instance, at 08:00 the ETC delivers 3397 W versus 706.8 W for the FPC, an enhancement of approximately 381%. Both collectors reach their highest outputs around midday as $T_{amb}$ approaches its maximum. The ETC peaks at 19,747 W at 13:00, which is about 46% higher than the FPC peak of 13,566 W at the same hour.

During the hottest part of the day (12:00–15:00), the ETC consistently maintains an advantage between 35% and 55%, reflecting its lower heat losses and better performance at higher operating temperatures. In the late afternoon, useful heat decreases sharply for both collectors as solar intensity declines, dropping to zero after 19:00. Across the full day, the ETC produces between 3 to 5.6 times more useful heat in the early morning and 35–55% more during peak solar hours, demonstrating its superior capability to sustain high thermal output under the hot, high-irradiance conditions typical of North Africa.

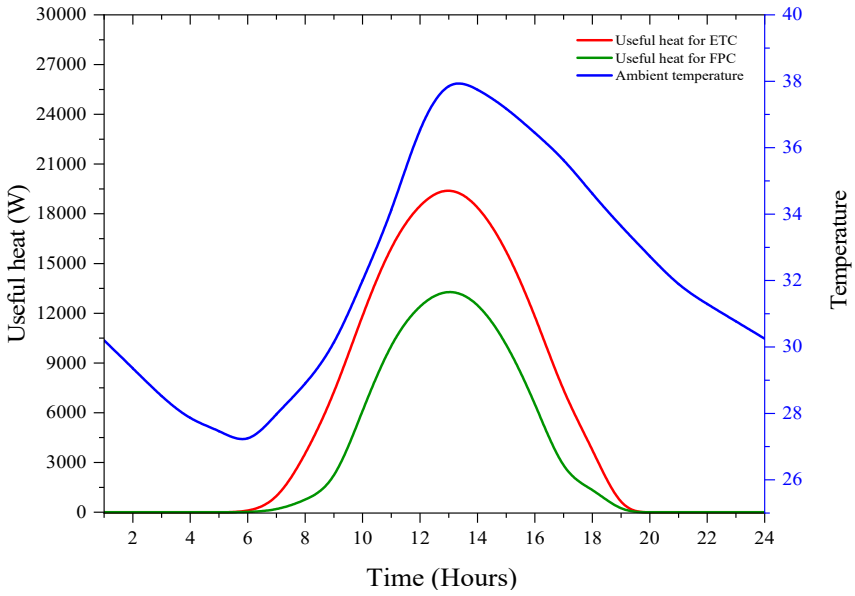


**Figure 3.** Hourly useful heat output of ETC and FPC with ambient temperature (Tlemcen, 18 July 2024).

Figure 4 illustrates the daily variation of generator heat rate for both FPC and ETC. Throughout the day, the ETC consistently delivers higher heat rates, reflecting its superior thermal performance. In the early morning (01:00–06:00), the ETC provides 8.09–10.01 kW, compared to 6.39–6.70 kW for the FPC, representing an improvement of ~27–50%. As solar irradiance increases, both systems' heat rates rise, but the ETC maintains a clear advantage. During peak hours (09:00–16:00), the ETC achieves generator heat rates of 9.33–17.16 kW, while the FPC ranges from 6.37–12.27 kW, corresponding to an enhancement of ~35–50%, ensuring a higher and more stable thermal input during maximum cooling demand. In the late afternoon and evening (17:00–24:00), the ETC continues to outperform the FPC, with relative improvements reaching ~50–65%, particularly as solar input declines, demonstrating its superior efficiency and heat retention under lower irradiance conditions. Consequently, the ETC provides a substantial and consistent improvement in generator heat rate throughout the day, ranging from approximately 25% in the early morning to 60% at night, highlighting its superior ability to supply the absorption chiller with reliable thermal energy under Tlemcen's high-irradiance conditions.

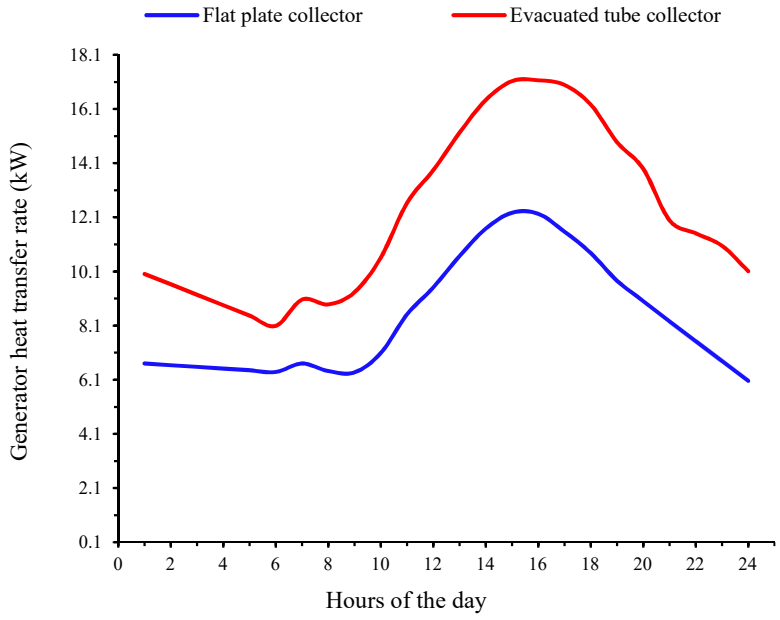


**Figure 4.** Hourly variation of generator heat supplied by FPC and ETC.

The hourly COP variations of the FPC and ETC throughout the day are illustrated in Figure 5. During the early morning hours (01:00–06:00), both collectors show similar COP values, with the FPC slightly higher (0.776–0.777) compared to the ETC (0.769–0.775), reflecting a minimal difference of about 0.7–1%. This indicates that under low solar irradiance, both collectors provide sufficient thermal input for the absorption chiller to operate efficiently. In the morning (07:00–09:00), the COP difference remains small, around 0.004–0.005, as both systems gradually increase their thermal output.

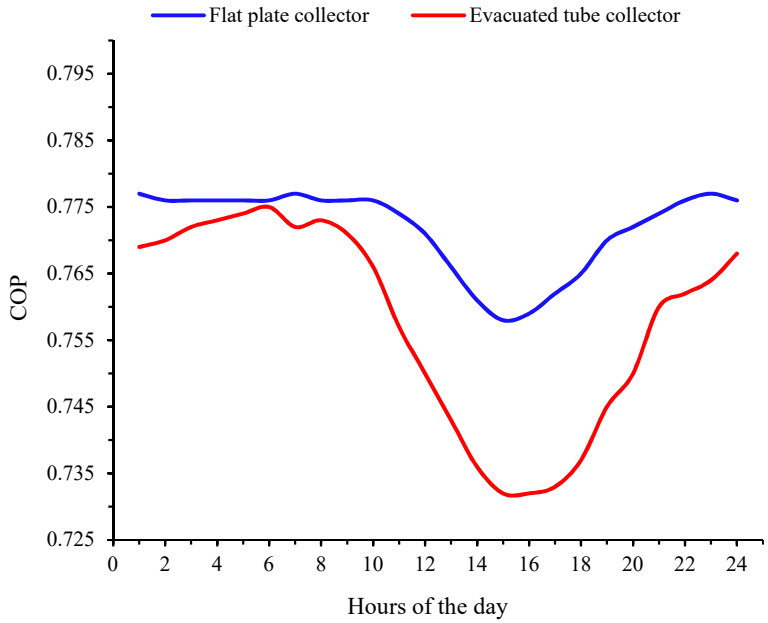


**Figure 5.** Diurnal COP profiles of the investigated system operating with FPC and ETC.

During peak solar hours (10:00–16:00), the FPC maintains a higher COP, decreasing moderately from 0.776 to 0.759, whereas the ETC declines more sharply from 0.766 to 0.732, corresponding to a difference of ~3–4%. Despite the ETC supplying higher generator heat rates during this period, the slightly lower COP reflects increased exergy losses due to higher generator temperatures. In the late afternoon and evening (17:00–24:00), the ETC COP gradually recovers from 0.733 to 0.768, while the FPC remains relatively stable between 0.762 and 0.776, showing that the COP gap narrows as thermal loads decrease. In general, the FPC delivers a slightly higher COP for most of the day, particularly during periods of intense solar irradiance, while the ETC provides a greater thermal input to the generator, albeit with a modest reduction in operational efficiency.

As seen in Figure 6, the absorption chiller's daily cooling capacity provided by the FPC and ETC shows a distinct performance variation throughout the day. The ETC consistently delivers higher cooling output than the FPC, reflecting its superior thermal energy supply to the generator. In the early morning hours 01:00–06:00, the ETC provides 6.27–7.70 kW compared to 4.96–5.20 kW for the FPC, representing an increase of approximately 25–50%, ensuring effective cooling from the start of the day. During peak solar hours 10:00–16:00, the ETC sustains cooling capacities of 8.13–12.56 kW, while the FPC delivers 5.50–9.31 kW, corresponding to an improvement of 30–35%, demonstrating the ETC's ability to meet high cooling demand during maximum irradiance. In the late afternoon and evening 17:00–24:00, the ETC continues to outperform the FPC, providing 7.77–12.46 kW versus 4.70–8.82 kW, highlighting superior heat retention and extended cooling capability. Therefore, although the FPC maintains slightly higher COP during peak hours, the ETC significantly enhances daily cooling performance, offering higher and more stable output under Tlemcen's high-irradiance conditions and proving to be the more effective choice for sustained and elevated cooling requirements.

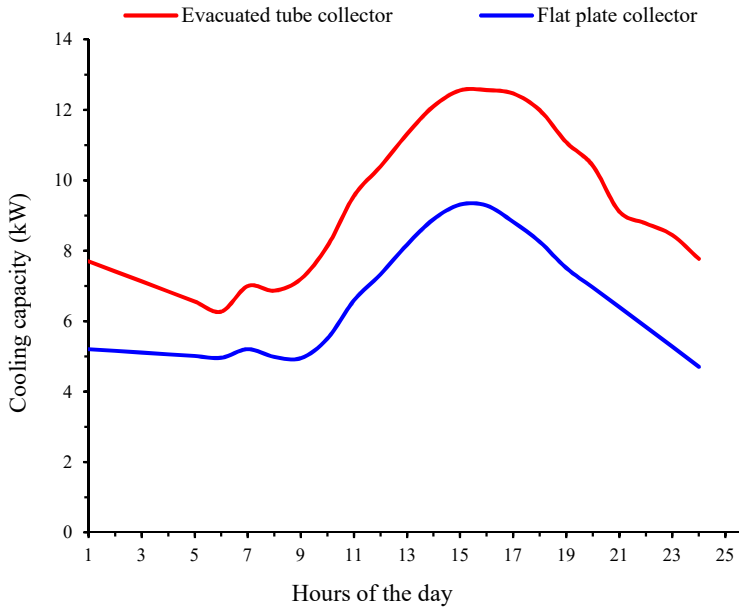


**Figure 6.** Time-resolved cooling performance of the absorption system for both investigated solar collectors.

The hourly variation of exergetic efficiency for the FPC and the ETC (Figure 7) reveals a persistent and measurable performance gap throughout the day. During the early hours (01:00–06:00), the FPC efficiency increases from 0.2639 to 0.2690, while the ETC rises from 0.2212 to 0.2436. Over this interval, the FPC maintains a 16–19% higher exergetic efficiency, reflecting lower irreversibilities under low-temperature operation. Between 07:00 and 09:00, both systems adjust as solar input becomes significant. The FPC ranges between 0.2639 and 0.2692, whereas the ETC fluctuates between 0.2316 and 0.2285. Here, the FPC advantage stabilizes at ~14–17%, highlighting its stronger thermodynamic robustness under moderate thermal loading.

Much sharper divergence appears during the main solar window (10:00–16:00), when temperatures are highest and entropy generation intensifies. The FPC decreases from 0.2578 to 0.2010, while the ETC drops more abruptly from 0.2152 to 0.1698. Throughout these hours, the FPC outperforms the ETC by 20–25%, indicating that higher ETC outlet temperatures drive greater exergy destruction, despite their benefit for heat gain. As the day transitions into late afternoon and night (17:00–24:00), both systems gradually recover. The FPC rises from 0.2065 to 0.2746, and the ETC increases from 0.1706 to 0.2202. Even during this recovery, the FPC consistently maintains a 22–25% advantage, showing that lower collector operating temperatures in this period reduce exergy losses more effectively in the FPC system. Overall, the FPC maintains higher exergetic efficiency than the ETC throughout all 24 hours, with an advantage of about 10–20%. Although the ETC provides more thermal energy, its higher operating temperatures increase irreversibilities. Consequently, the FPC delivers better-quality useful energy to the absorption system.

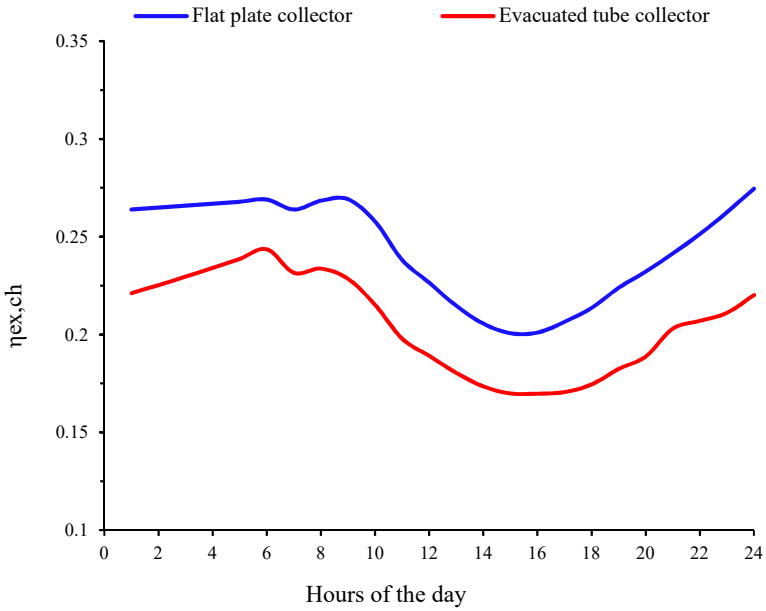


**Figure 7.** Daily exergetic efficiency values of FPC and ETC over 24 hours.

The generator irreversibility results in Figure 8 show that the ETC produces consistently higher exergy losses than the FPC across all 24 hours, with a well-defined quantitative gap. During the early morning (hours 1–6), ETC losses exceed those of the FPC by 27–49%, increasing from a 49% difference at hour 1 (6.701 vs 10.01 kW) to 27% at hour 6 (6.383 vs 8.091 kW). Between hours 7 and 12, as solar input strengthens, the FPC increases from 6.711 to 9.511 kW while the ETC rises from 9.062 to 13.84 kW, corresponding to 29–45% higher irreversibilities for the ETC.

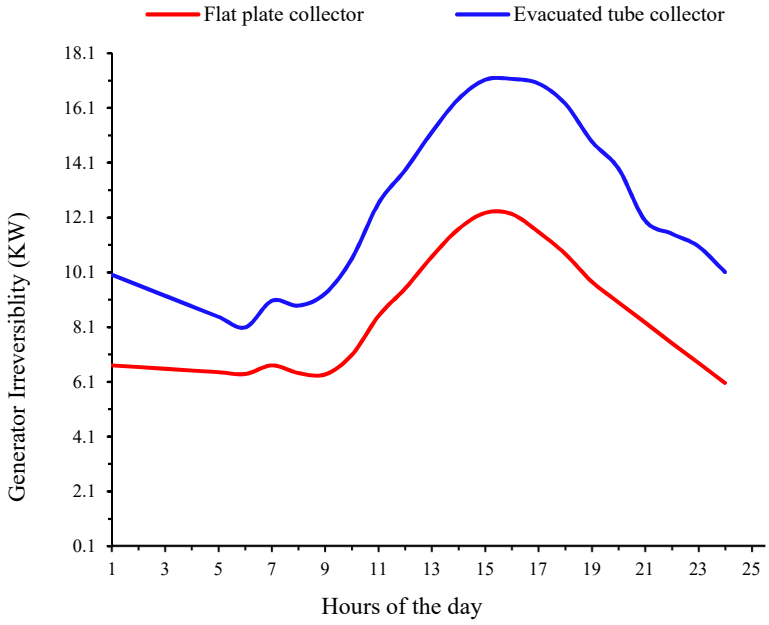


**Figure 8.** Comparison of hourly generator irreversibilities between FPC and ETC.

During the peak thermal period (hours 13–16), the FPC ranges between 10.67 and 12.23 kW, whereas the ETC reaches 15.22–17.16 kW, maintaining differences of 36–43%. In the evening (hours 17–24), the gap widens further, with ETC losses exceeding those of the FPC by 26–66%, reaching the maximum difference at hour 24 (6.06 vs 10.07 kW, +66%). Overall, the ETC shows approximately 26% to 66% higher generator exergy losses compared with the FPC across the full day, indicating that the higher operating temperatures characteristic of ETC-driven generation intensify entropy production and magnify irreversibilities.

Figure 9 shows the daily changes in total exergy loss for the investigated single-effect LiBr–$H_2O$ system. At the start of the day (hours 1–6), the ETC exhibits lower losses, 3.199–3.36 kW, compared to the FPC, 3.523–3.562 kW, corresponding to reductions of 8–10% due to its higher and more uniform thermal supply, which minimizes irreversibilities in the generator and absorber. From hours 7–10, losses increase moderately, with the ETC remaining slightly lower (3.255–3.274 kW) than the FPC (3.523–3.558 kW), reflecting stable heat delivery under rising solar irradiance. During peak hours (11–16), the ETC experiences a sharp rise in exergy loss, reaching a maximum of 6.317 kW at hour 16, roughly 1.63 times higher than the FPC peak of 3.863 kW, due to elevated operating

temperatures that, while boosting thermal input and cooling capacity, amplify entropy generation. From hours 17–20, the ETC losses gradually decline (6.231–4.757 kW) but remain higher than the FPC (3.586–3.261 kW). In the late evening (hours 21–24), the ETC further decreases to 3.131 kW, about 13% lower than the FPC (3.604 kW), as moderate temperatures restore more efficient operation.

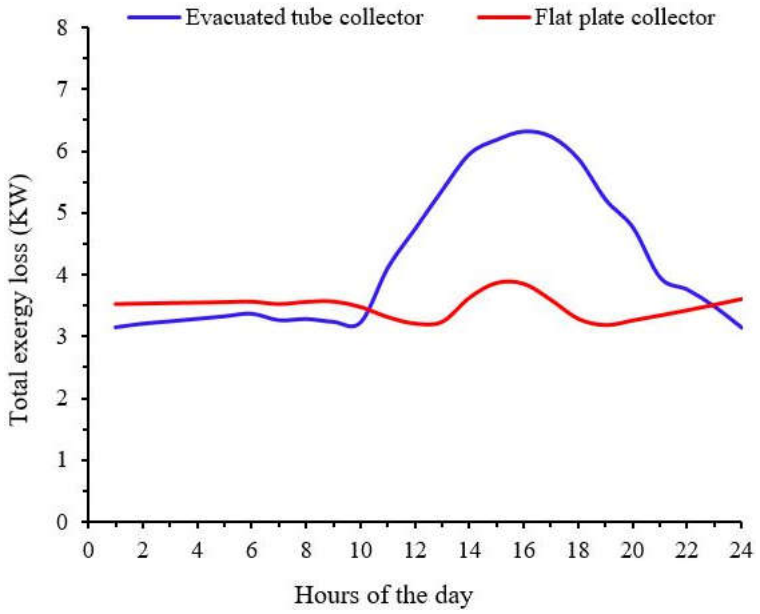


**Figure 9.** Daily variation in total exergy loss for FPC and ETC.

Figure 10 clearly indicates that the solar collector is the primary source of exergy loss in the system, followed by the generator and absorber. On the other hand, components such as the condenser, evaporator, solution pump, and expansion valves exhibit relatively low energy loss values, indicating better thermodynamic performance.

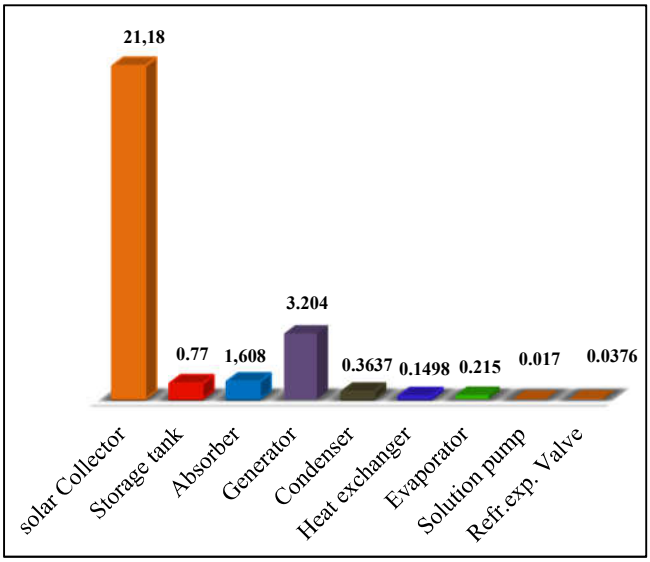


**Figure 10.** *Exergy destruction on the system*

## 4. Conclusions

This study investigated the thermodynamic performance of a single-effect LiBr–$H_2O$ SACS operating under typical summer climatic conditions of Tlemcen, Algeria. The system integrates a solar collector field, thermal storage tank, and standard absorption cycle components, and two solar technologies, FPC ETC), were comparatively assessed using hourly dynamic energy and exergy analyses.

The numerical model was validated against published reference data, showing deviations below 1.62% for exergetic efficiency, and 1.11% for the COP, confirming the reliability of the model in predicting system behavior under realistic operating conditions. Hourly simulations captured the temporal evolution of thermal output, cooling capacity, and irreversibilities in response to variations in solar irradiance and ambient temperature.

Exergy analysis revealed that the solar collector is the dominant source of irreversibility, accounting for approximately 79% of the collector input and 16% of total system exergy destruction,

The comparative analysis demonstrated that the ETC significantly outperforms the FPC in terms of thermal delivery and cooling performance throughout the day. In the early morning, the ETC provided 3–5.6 times higher useful heat and 25–50% greater cooling capacity, while during peak solar hours it maintained 35–55% higher thermal output and 30–35% superior cooling performance. Although the ETC exhibited 10–25% lower exergetic efficiency due to increased generator temperatures and associated entropy generation, its enhanced heat supply resulted in higher and more stable cooling production. Generator exergy losses were 26–66% higher with the ETC; however, this drawback was outweighed by the overall system performance gains.

The results indicate that optimization of the solar collector subsystem offers the greatest potential for performance improvement, followed by enhancements in generator and absorber design. Considering daily cooling capacity, thermal energy availability, and exergy destruction, the ETC configuration is identified as the most suitable option for SACSs operating under high-irradiance North African climatic conditions.

## Author contributions

CRediT: Bilal ABDESSELAM: Conceptualization, Methodology, Formal Analysis, Investigation, Software, Visualization, writing—Original Draft; Mohammed Benramdane: Data curation, investigation, resources, validation, writing—review & editing; Abdennour Aliane: Methodology, Supervision, Project Administration, Validation, writing—Review & Editing; Mohammed El Amine Chikh: Resources, data curation, formal analysis, visualization, writing—review & editing.

## Declaration of Competing Interest

The authors declare that they have no known financial or personal relationships that could have influenced the work reported in this paper.

**Data availability**

Data will be made available on request.

**References**

[1] Qasem, R. H. M., & Scholz, M. (2025). Climate change impact on resources in the MENA region: a systematic and critical review. *Physics and Chemistry of the Earth, Parts A/B/C*, 103936. https://doi.org/10.1016/j.pce.2025.103936

[2] Rahman, S. M., Raihan, A., Alam, M. S., & Chowdhury, S. (2025). Greenhouse gas emission dynamics and climate change mitigation efforts toward sustainability in the Middle East and North Africa (MENA) region. *Regional Sustainability*, *6*(4), 100246. https://doi.org/10.1016/j.regsus.2025.100246

[3] Malik, A., Stenchikov, G., Mostamandi, S., Parajuli, S., Lelieveld, J., Zittis, G., ... & Usman, M. (2024). Accelerated historical and future warming in the Middle East and North Africa. *Journal of Geophysical Research: Atmospheres*, *129*(22), e2024JD041625. https://doi.org/10.1029/2024JD041625

[4] Sahabi-Abed, S. (2022). Assessment of future climate projections in Algeria using statistical downscaling model. *International Journal of Big Data Mining for Global Warming*, *4*(01), 2130001. https://doi.org/10.1142/S2630534821300013

[5] Salata, F., Falasca, S., Ciancio, V., Curci, G., & de Wilde, P. (2023). Climate-change related evolution of future building cooling energy demand in a Mediterranean Country. *Energy and Buildings*, *290*, 113112. https://doi.org/10.1016/j.enbuild.2023.113112

[6] Robei, S., Settou, N., Fellah, M., Negrou, B., Yao, J., Bouferrouk, A., ... & El-Hiti, G. A. (2025). Analyzing the force drivers and trends of energy consumption in the non-energy industrial sector: A comprehensive exploration. *Journal of Cleaner Production*, *525*, 146648. https://doi.org/10.1016/j.jclepro.2025.146648

[7] Sahnoune, F., Imessad, K., & Bouakaz, D. M. (2017, February). Energy consumption renewable energy development and environmental impact in Algeria-Trend for 2030. *AIP Conference Proceedings*, *1814*(1), 020072). https://doi.org/10.1063/1.4976291

[8] Bélaïd, F., & Youssef, M. (2017). Environmental degradation, renewable and non-renewable electricity consumption, and economic growth: Assessing the evidence from Algeria. *Energy policy*, *102*, 277-287. https://doi.org/10.1016/j.enpol.2016.12.012

[9] Tian, Y., & Zhao, C. Y. (2013). A review of solar collectors and thermal energy storage in solar thermal applications. *Applied Energy*, *104*, 538-553. https://doi.org/10.1016/j.apenergy.2012.11.051

[10] Tsalikis, G., & Martinopoulos, G. (2015). Solar energy systems potential for nearly net zero energy residential buildings. *Solar Energy*, *115*, 743-756. https://doi.org/10.1016/j.solener.2015.03.037

[11] Ibrahim, N. I., Yahiaoui, A., Garkuwa, J. A., Mansour, R. B., & Rehman, S. (2024). Solar cooling with absorption chillers, thermal energy storage, and control strategies: A review. *Journal of Energy Storage*, *97*, 112762. https://doi.org/10.1016/j.est.2024.112762

[12] Jadhav, A., Raut, D., & Kalamkar, V. R. (2025). Review on solar powered $H_2O$-LiBr absorption cooling systems for sustainable buildings. *Journal of Building Engineering*, 114015. https://doi.org/10.1016/j.jobe.2025.114015

[13] Aliane, A., Abboudi, S., Seladji, C., & Guendouz, B. (2016). An illustrated review on solar absorption cooling experimental studies. *Renewable and Sustainable Energy Reviews*, *65*, 443-458. https://doi.org/10.1016/j.rser.2016.07.012

[14] Kalogirou, S. (2003). The potential of solar industrial process heat applications. *Applied Energy*, *76*(4), 337-361. https://doi.org/10.1016/S0306-2619(02)00176-9

[15] Chen, E., Zhao, Y., Wang, M., Bian, M., Cai, W., Li, B., & Dai, Y. (2023). Experimental investigation of a solar-assisted absorption-compression system for heating and cooling. *Solar Energy*, *257*, 18-33. https://doi.org/10.1016/j.solener.2023.04.025

[16] Jalalizadeh, M., Fayaz, R., Delfani, S., Mosleh, H. J., & Karami, M. (2021). Dynamic simulation of a trigeneration system using an absorption cooling system and building integrated photovoltaic thermal solar collectors. *Journal of Building Engineering*, *43*, 102482. https://doi.org/10.1016/j.jobe.2021.102482

[17] Patiño-Jaramillo, G. A., Rivera-Alvarez, A., & Osorio, J. D. (2023). Performance evaluation and optimal design analysis of continuous-operation solar-driven cooling absorption systems with thermal energy storage. *Journal of Thermal Science and Engineering Applications*, *15*(12), 121009.

https://doi.org/10.1115/1.4063409

[18] Bellos, E., Arabkoohsar, A., Lykas, P., Sammoutos, C., Kitsopoulou, A., & Tzivanidis, C. (2024). Investigation of a solar-driven absorption heat transformer with various collector types for industrial process heating. *Applied Thermal Engineering*, *244*, 122665. https://doi.org/10.1016/j.applthermaleng.2024.122665

[19] Lahoud, C., El Brouche, M., Lahoud, C., & Hmadi, M. (2021). A Review of single-effect solar absorption chillers and its perspective on Lebanese case. *Energy Reports*, *7*, 12-22. https://doi.org/10.1016/j.egyr.2021.09.052

[20] Wang, J., Yan, R., Wang, Z., Zhang, X., & Shi, G. (2018). Thermal performance analysis of an absorption cooling system based on parabolic trough solar collectors. *Energies*, *11*(10), 2679. https://doi.org/10.3390/en11102679

[21] Zhou, Y., Pan, L., Han, X., & Sun, L. (2023). Dynamic modeling and thermodynamic analysis of lithium bromide absorption refrigeration system using Modelica. *Applied Thermal Engineering*, *225*, 120106. https://doi.org/10.1016/j.applthermaleng.2023.120106

[22] Tariq, H. A., Altamirano, A., Collignon, R., Stutz, B., & Coronas, A. (2025). Experimental study on the effect of an ionic liquid as anti-crystallization additive in a bi-adiabatic $H_2O$-LiBr absorption chiller prototype. *Applied Thermal Engineering*, *259*, 124756. https://doi.org/10.1016/j.applthermaleng.2024.124756

[23] Saleh, A., & Mosa, M. (2014). Optimization study of a single-effect water–lithium bromide absorption refrigeration system powered by flat-plate collector in hot regions. *Energy Conversion and Management*, *87*, 29-36. https://doi.org/10.1016/j.enconman.2014.06.098

[24] Izquierdo, M., González-Gil, A., & Palacios, E. (2014). Solar-powered single-and double-effect directly air-cooled LiBr–$H_2O$ absorption prototype built as a single unit. *Applied Energy*, *130*, 7-19. https://doi.org/10.1016/j.apenergy.2014.05.028

[25] Gomri, R. (2013). Simulation study on the performance of solar/natural gas absorption cooling chillers. *Energy Conversion and Management*, *65*, 675-681. https://doi.org/10.1016/j.enconman.2011.10.030

[26] Migla, L., Bogdanovics, R., & Lebedeva, K. (2023). Performance improvement of a solar-assisted absorption cooling system integrated with latent heat thermal energy storage. *Energies*, *16*(14), 5307. https://doi.org/10.3390/en16145307

[27] Zhu, H., Guo, B., Geng, W., Chi, J., & Guo, S. (2022). Simulation of an improved solar absorption refrigeration system with phase change materials. *Energy reports*, *8*, 3671-3679. https://doi.org/10.1016/j.egyr.2022.02.306

[28] Bouguetaia, N., Bellel, N., & Lekbir, A. (2023). Absorption Chiller system driven by the solar hybrid system: case study in the algeria weather condition. Journal of Thermal Science and Engineering Applications, 15(6), 061009.

https://doi.org/10.1115/1.4062125

[29] Salameh, T., Alkhalidi, A., Rabaia, M. K. H., Al Swailmeen, Y., Alroujmah, W., Ibrahim, M., & Abdelkareem, M. A. (2022). Optimization and life cycle analysis of solar-powered absorption chiller designed for a small house in the United Arab Emirates using evacuated tube technology. *Renewable Energy*, *198*, 200-212. https://doi.org/10.1016/j.renene.2022.07.121

[30] Assilzadeh, F., Kalogirou, S. A., Ali, Y., & Sopian, K. (2005). Simulation and optimization of a LiBr solar absorption cooling system with evacuated tube collectors. *Renewable Energy*, *30*(8), 1143-1159. https://doi.org/10.1016/j.renene.2004.09.017

[31] Li, Z., Ye, X., & Liu, J. (2014). Performance analysis of solar air cooled double effect LiBr/$H_2O$ absorption cooling system in subtropical city. *Energy Conversion and Management*, *85*, 302-312. https://doi.org/10.1016/j.enconman.2014.05.095

[32] Lior, N., & Zhang, N. (2007). Energy, exergy, and second law performance criteria. *Energy*, *32*(4), 281-296. https://doi.org/10.1016/j.energy.2006.01.019

[33] Rodríguez-Muñoz, J. L., Ramírez-Minguela, J. J., Ituna-Yudonago, J. F., & González-Hernández, I. J. (2025). Performance improvement by rectifier heat integration in an alternative absorption-compression hybrid refrigeration system. *Applied Thermal Engineering*, 127139. https://doi.org/10.1016/j.applthermaleng.2025.127139

[34] Hasan, A. A., Goswami, D. Y., & Vijayaraghavan, S. (2002). First and second law analysis of a new power and refrigeration thermodynamic cycle using a solar heat source. *Solar Energy*, *73*(5), 385-393. https://doi.org/10.1016/S0038-092X(02)00113-5

[35] Joybari, M. M., & Haghighat, F. (2016). Exergy analysis of single effect absorption refrigeration systems: The heat exchange aspect. *Energy Conversion and Management*, *126*, 799-810. https://doi.org/10.1016/j.enconman.2016.08.029

[36] Kerme, E. D., Chafidz, A., Agboola, O. P., Orfi, J., Fakeeha, A. H., & Al-Fatesh, A. S. (2017). Energetic and exergetic analysis of solar-powered lithium bromide-water absorption cooling system. *Journal of Cleaner Production*, *151*, 60-73. https://doi.org/10.1016/j.jclepro.2017.03.060

[37] Sahli, H., Hammemi, R., Elakhdar, M., Tashtoush, B., & Nehdi, E. (2025). Comparative performance study of a novel heat driven absorption cooling system incorporating a turbo-compressor. *International Communications in Heat and Mass Transfer*, *164*, 108906. https://doi.org/10.1016/j.icheatmasstransfer.2025.108906

[38] Arora, A., & Kaushik, S. C. (2009). Theoretical analysis of LiBr/$H_2O$ absorption refrigeration systems. *International Journal of Energy Research*, *33*(15), 1321-1340. https://doi.org/10.1002/er.1542

[39] Bellos, E., Tzivanidis, C., & Antonopoulos, K. A. (2016). Exergetic, energetic and financial evaluation of a solar driven absorption cooling system with various collector types. *Applied Thermal Engineering*, *102*, 749-759. https://doi.org/10.1016/j.applthermaleng.2016.04.032

[40] Bellos, E., Tzivanidis, C., Symeou, C., & Antonopoulos, K. A. (2017). Energetic, exergetic and financial evaluation of a solar driven absorption chiller–A dynamic approach. *Energy Conversion and Management*, *137*, 34-48. https://doi.org/10.1016/j.enconman.2017.01.041

[41] Ahmadi, P., Dincer, I., & Rosen, M. A. (2013). Thermodynamic modeling and multi-objective evolutionary-based optimization of a new multigeneration energy system. *Energy Conversion and Management*, *76*, 282-300. https://doi.org/10.1016/j.enconman.2013.07.049

[42] Greco, A., Gundabattini, E., Gnanaraj, D. S., & Masselli, C. (2020). A comparative study on the performances of flat plate and evacuated tube collectors deployable in domestic solar water heating systems in different climate areas. *Climate*, *8*(6), 78. https://doi.org/10.3390/cli8060078